JACS
JOURNAL OF THE AMERICAN CHEMICAL SOCIETY

Article

pubs.acs.org/JACS

Controllable Perovskite Crystallization at a Gas–Solid Interface for Hole Conductor-Free Solar Cells with Steady Power Conversion Efficiency over 10%

Feng Hao,[†] Constantinos C. Stoumpos,[†] Zhao Liu,[‡] Robert P. H. Chang,[‡] and Mercouri G. Kanatzidis*,[†]

[†]Department of Chemistry, and [‡]Department of Materials Science and Engineering, and Argonne-Northwestern Solar Energy Research (ANSER) Center, Northwestern University, 2145 Sheridan Road, Evanston, Illinois 60208, United States

Supporting Information

ABSTRACT: Depositing a pinhole-free perovskite film is of paramount importance to achieve high performance perovskite solar cells, especially in a heterojunction device format that is free of hole transport material (HTM). Here, we report that high-quality pinhole-free $CH_3NH_3PbI_3$ perovskite film can be controllably deposited via a facile low-temperature (<150 °C) gas–solid crystallization process. The crystallite formation process was compared with respect to the conventional solution approach, in which the needle-shaped solvation intermediates ($CH_3NH_3PbI_3$·DMF and $CH_3NH_3PbI_3$·H_2O) have been recognized as the main cause for the incomplete coverage of the resultant film. By avoiding these intermediates, the films crystallized at the gas–solid interface offer several beneficial features for device performance including high surface coverage, small surface roughness, as well as controllable grain size. Highly efficient HTM-free perovskite solar cells were constructed with these pinhole-free $CH_3NH_3PbI_3$ films, exhibiting significant enhancement of the light harvesting in the long wavelength regime with respect to the conventional solution processed one. Overall, the gas–solid method yields devices with an impressive power conversion efficiency of 10.6% with high reproducibility displaying a negligible deviation of 0.1% for a total of 30 cells.

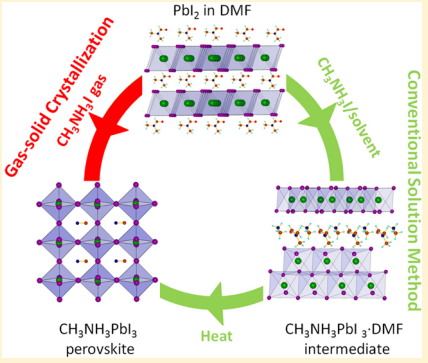

INTRODUCTION

Organic–inorganic hybrid perovskites have gained considerable research attention during the past two years and have revolutionized the prospects of emerging photovoltaic technologies, in forms of both light harvesters[1−4] and hole transport materials.[5−7] These organic–inorganic hybrid perovskite compounds adopt the ABX_3 perovskite structure, which consists of a network of corner-sharing BX_6 octahedra, where the B atom is a divalent metal cation (typically Ge^{2+}, Sn^{2+}, or Pb^{2+}) and X is a monovalent anion (typically F^-, Cl^-, Br^-, or I^-); the A cation is selected to balance the total charge, and it can be a Cs^+ or a small molecular species.[8−10] Such perovskites afford several important features including excellent optical properties that are tunable by controlling the chemical compositions,[11,12] ambipolar charge transport,[13] and long electron and hole diffusion lengths.[14,15] Solar cells based on these perovskites have gained enormous significance and reached a power conversion efficiency close to 20%,[1,3,4,16] approaching the efficiency of commercialized c-Si solar cells and thin film photovoltaic solar cells such as CdTe and $Cu_2ZnSn(Se,S)_4$.[17]

Currently, four main device architectures have been explored in these perovskite solar cells. First is the so-called "sensitizing" architecture, where the perovskite simply acts as a light absorber coating a semiconducting mesoporous layer of TiO_2 or ZnO nanoparticles. In addition to acting as a structure-directing support, these semiconducting mesoporous scaffolds also are responsible for accepting electrons from the perovskite and transporting them to the collecting electrode.[4,13,18,19] Second is the meso-superstructured architecture, where an inert scaffold of alumina is used instead of the aforementioned semiconductor layer.[3,20] In these device architectures, excited electrons should be only transported through the perovskite due to the insulating nature of the alumina scaffold. Third is a planar thin-film heterojunction architecture lacking the mesoporous scaffold layer that has recently reported to have the highest conversion efficiencies, where the perovskite layer is utilized both as light absorber and as long-range transporter of both charge species.[15,16,21] The final is a hole-conductor free architecture, where the removal of a separate hole transporter material (HTM) layer means that all hole transport occurs through the perovskite itself.[6,7] The thin-film planar and mesostructured approaches should ultimately provide the highest efficiencies, because the interfacial area at these heterojunctions, where nonradiative recombination losses are most likely to occur, is significantly reduced.[22] While most research attention has been drawn into pursuing higher conversion efficiency of these perovskite solar cells via judicious interfacial engineering,[23−25] the material cost should also be considered as an important factor governing the practical application of this promising technology, where the HTM-free

Received: September 8, 2014
Published: November 6, 2014

   dx.doi.org/10.1021/ja509245x | J. Am. Chem. Soc. 2014, 136, 16411−16419

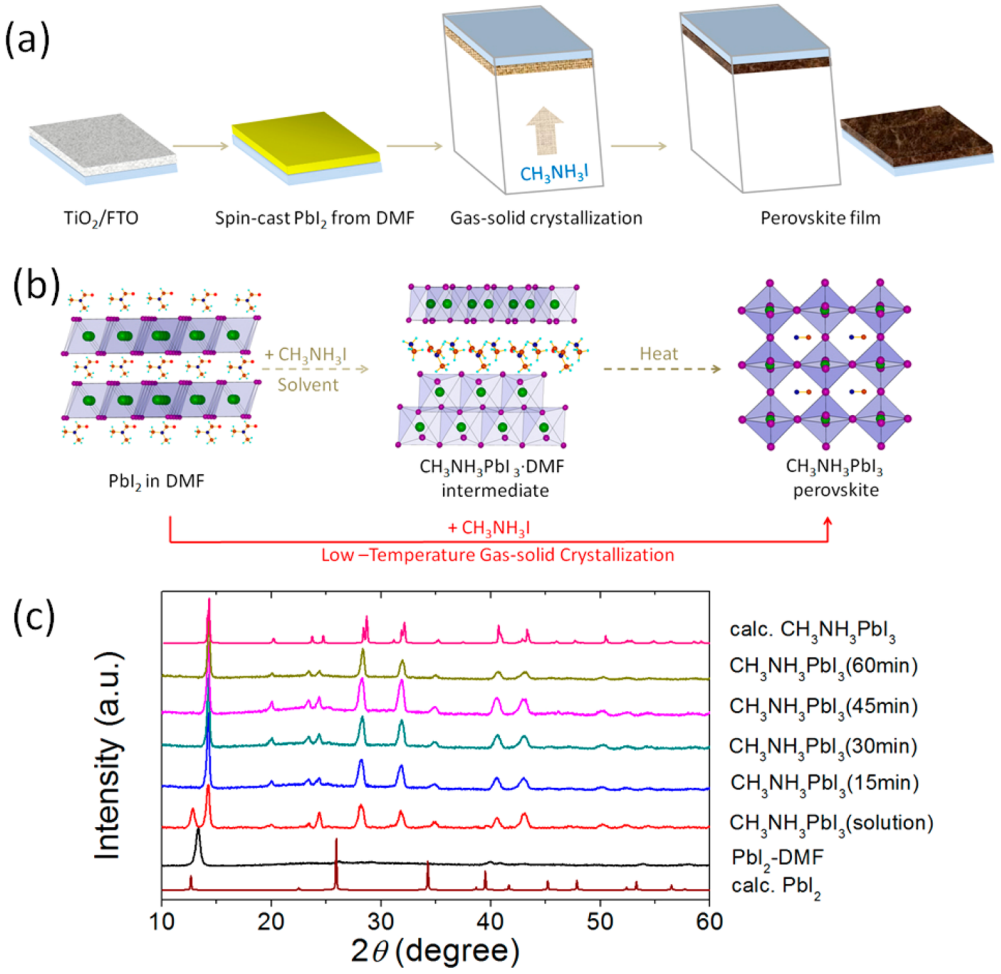

Figure 1. (a) Schematic gas–solid crystallization procedure for the pinhole-free perovskite film. (b) Crystal formation scheme for the perovskite material via conventional solution process, where the solvated $CH_3NH_3PbI_3$·DMF intermediate phase dominated the needle-shaped and incomplete coverage of the obtained film with pinholes. As indicated by the red arrow, our low-temperature gas–solid crystallization process effectively addresses this problem, leading to a high-quality pinhole-free perovskite film. (C) X-ray diffraction (XRD) patterns of the gas–solid crystallized perovskite films under 150 °C with a different reaction time. Patterns of a sequential solution processed perovskite film and the simulated standard one are also presented for comparison.

devices possess a substantial advantage by eliminating the need to employ an additional organic or inorganic HTM layer for the purpose of hole extraction.

In this regard, Etgar et al. first reported that $CH_3NH_3PbI_3$ perovskite nanocrystals could act both as a light harvester as well as a hole transporter in solar cells comprising a mesoscopic $CH_3NH_3PbI_3/TiO_2$ heterojunction.[6] This HTM-free heterojunction architecture bears a much simpler structure beneficial for reducing the cost and lowering the charge recombination possibility by minimizing the interfacial area. With efforts on the perovskite layer and back contact interfacial modification, a power conversion efficiency of 8.04% has been achieved by developing an efficient perovskite deposition method with a combination of different solvents.[7] It has been proposed that the HTM-free heterojunction architecture's lower performance most likely arises from pinhole formation, incomplete perovskite film coverage resulting in low-resistance shunting paths, as well as reduced light absorption in the solar cell. Any pinholes formed in the perovskite layer can compromise the efficiency by causing shunt paths in the device. Currently, the most commonly applied deposition methods for the perovskites layer are the sequential deposition from solution[4] and dual-source vapor evaporation.[21] In a typical sequential deposition process, the PbI_2 is first spin-coated from solution in dimethylformamide (DMF) or dimethyl sulfoxide (DMSO) onto the mesoporous titania film and subsequently transformed into the perovskite by dipping into a solution of methylammonium iodide (MAI), typically in isopropanol. Formation of perovskite is instantaneous within the mesoporous host upon contacting the two components.[26,27] By following this fabrication protocol for perovskite solution coating on mesoporous TiO_2 substrates, power conversion efficiencies up to 10% have been realized, reported by several independent research groups.[28−30] However, two major problems were found for sequential deposition on planar substrate: one is incomplete conversion of PbI_2 to perovskite, and the other is uncontrolled perovskite crystal growth as well as surface morphology,[31,32] thus leading to the poor reproducibility of the perovskite films as well as a large variation on the photovoltaic response. A vapor deposition method was also proposed to deposit extremely uniform perovskite film with crystalline platelets at nanometer scale.[33,34] However, this is a high energy-consuming process with respect to the cost-effective solution process and also limits the substrate choice.[35] More recently, a vapor-assisted solution process (VASP) has been developed for the deposition of perovskite absorbing layer, which is like a combination of the

dx.doi.org/10.1021/ja509245x | J. Am. Chem. Soc. 2014, 136, 16411−16419

aforementioned two methods.[31] Conversion efficiency over 12% has been obtained in a planar architecture with Spiro-OMeTAD as HTM. It has also been observed that PbI_2 impurity easily formed in the adjoining perovskite grains in this VASP process, which was probably due to the weakly orientation polarization between the organic and inorganic species in the hybrid perovskite.[36] Obviously, it is worth developing more efficient and reproducible HTM-free mesoscopic heterojunction perovskite solar cells using more controllable and versatile deposition methods for the perovskite layer.

Throughout the recent literature, it is apparent that the morphology of $CH_3NH_3PbI_3$ crystallites significantly impacts the film surface coverage and coloration of the devices as well as the electrical properties. A major issue in the solution-based fabricated devices, which currently hold the record efficiency value of 19.3%,[16] is the uncontrolled reproducibility of the device performance, which affords a wide range of efficiency distribution among devices prepared with identical fabrication protocols. In this study, we demonstrate that high-quality pinhole-free methylammomium lead triiodide ($CH_3NH_3PbI_3$) perovskite films can be deposited via a facile low-temperature (<150 °C) gas−solid crystallization reaction under inert atmosphere, but with better control on the film morphology and chemical composition than the previously reported VASP method. We show here that the perovskite film quality such as the particle size and surface coverage could be easily controlled by the film growth process. We show that the perovskite thin films undergo a grain coarsening process that leads to a controllable grain size. With respect to the conventional solution process, our gas−solid crystallization process effectively avoids the solvation and hydration processing or undesirable complex structural reorganization transitions. This enabled us to construct highly efficient and reproducible HTM-free perovskite solar cells with these pinhole-free $CH_3NH_3PbI_3$ films, exhibiting significant enhancement of the light harvesting in the long wavelength regime, in comparison to the devices with the solution deposited perovskite films, thus yielding a notable conversion efficiency of 10.6% along with a negligible standard deviation of 0.1% for a total of 30 cells.

RESULTS AND DISCUSSION

Perovskite Film Deposition. As shown in Figure 1a, the $CH_3NH_3PbI_3$ perovskite thin films were fabricated via a straightforward gas−solid crystallization reaction between the two components in a nitrogen filled glovebox, in which the PbI_2 framework was first spin-cast from a DMF solution on the mesoporous TiO_2 layer, and subsequently converted to perovskite by a gas−solid crystallization process in a closed container. This process directly avoids the formation of the needle-forming solvated $CH_3NH_3PbI_3$·DMF intermediate phase, as indicated by the crystal formation scheme in Figure 1b. Unlike the previously reported VASP process, direct contact between the CH_3NH_3I powder and the PbI_2 framework is avoided by facing down the PbI_2-infiltrated TiO_2 electrodes at a constant height of around 2 in. against the CH_3NH_3I powder, which is more similar to the setup of commercial vapor evaporation equipment.[21] Our design provides excellent control of the perovskite crystal growth rate and film coverage including the CH_3NH_3I precursor loading amounts, the atmosphere, and the reaction temperature and time. The detailed film deposition and device fabrication procedure are described in the Supporting Information.

The method employed here takes advantage of the fact that CH_3NH_3I is a stable adduct of two gases, CH_3NH_2 and HI. Despite the fact that the total decomposition temperature of the CH_3NH_3I salt lies in the 280−350 °C range, as determined by thermogravimetric analysis (see Figure S1 in the Supporting Information), the vapor pressure of the individual gases is sufficient to generate enough molecules of CH_3NH_2 and HI in the gaseous phase for the PbI_2 conversion to $CH_3NH_3PbI_3$ to proceed at a controlled rate. This can be further tuned by careful control of the decomposition temperature (100−150 °C was used in this report). The method offers several positive features; because the reaction proceeds at the solid−gas interface, the presence of adventitious solvent molecules is strictly avoided. Moreover, the method promises control over the grain size of the crystallites during the crystal growth process with particle size and film surface coverage being tunable parameters based on the evaporation time and temperature.

The composition and morphology evolution of the perovskite film along the gas−solid crystallization process are first investigated by a series of X-ray diffraction (XRD) and scanning electron microscopy (SEM) measurements with different reaction time. All of the films were deposited on mesoporous TiO_2 electrodes to ensure the condition comparable to that of the working device. As shown in Figure 1c, the strong Bragg peaks at 14.08°, 28.41°, 31.85°, and 43.19° can be assigned to (110), (220), (310), and (330) of the $CH_3NH_3PbI_3$ crystal, corresponding to a tetragonal *I4cm* crystal structure of halide perovskite with high crystallinity.[2,37] The XRD pattern of a sequential solution processed perovskite film is also presented for comparison. Notably, a signature peak at 12.65° indicates the incompletely converted PbI_2.[4] Such PbI_2 impurity has been widely observed even in the highly efficient devices from the sequential deposition method.[4,38] The absence of this peak in the present gas−solid crystallized perovskite film suggests complete conversion of the PbI_2 precursor. Interestingly, the XRD pattern of the as-deposited PbI_2 films from DMF solution suggested the presence of a slightly modified PbI_2 phase with larger lattice parameter (2θ = 13.24°) as compared to the calculated pattern of PbI_2 (2θ = 12.65°).[39] A possible explanation is that PbI_2 is composed of planes of Pb^{2+} ions sandwiched between adjacent layers of hexagonally arranged iodide ions forming extended 2D layers held together by van der Waals interactions. The interlayer space of ∼2.66 Å is large enough to host a variety of small molecules such as the remnant DMF molecules from the solution processing, and it can even form stable adducts such as PbI_2·DMF.[39] The ease of intercalation of different guest molecules can result in a lattice expansion along the *c* axis, and it is also responsible for the high reactivity of PbI_2 upon addition of the CH_3NH_3I solutions.[40] Very recently, it has been shown that the DMSO solvent can form stable solvates with $CH_3NH_3PbI_3$, possibly $CH_3NH_3PbI_3$·DMSO, thus facilitating the crystallization process of the perovskite layer.[41] The crystal structure of $CH_3NH_3PbI_3$·DMSO is expected to be similar to those of $CH_3NH_3PbI_3$·DMF and $CH_3NH_3PbI_3$·H_2O, which are discussed below. These intermediate phases are more reactive than PbI_2 itself and facilitate the subsequent crystallization process of the corresponding perovskite film.

The importance of controlling the interfacial layers in the solar cell devices is apparent. First, a local interfacial order at the titania/perovskite interface promoted by specific local interactions has been demonstrated.[42] Second, a built-in electric

dx.doi.org/10.1021/ja509245x | J. Am. Chem. Soc. 2014, 136, 16411−16419

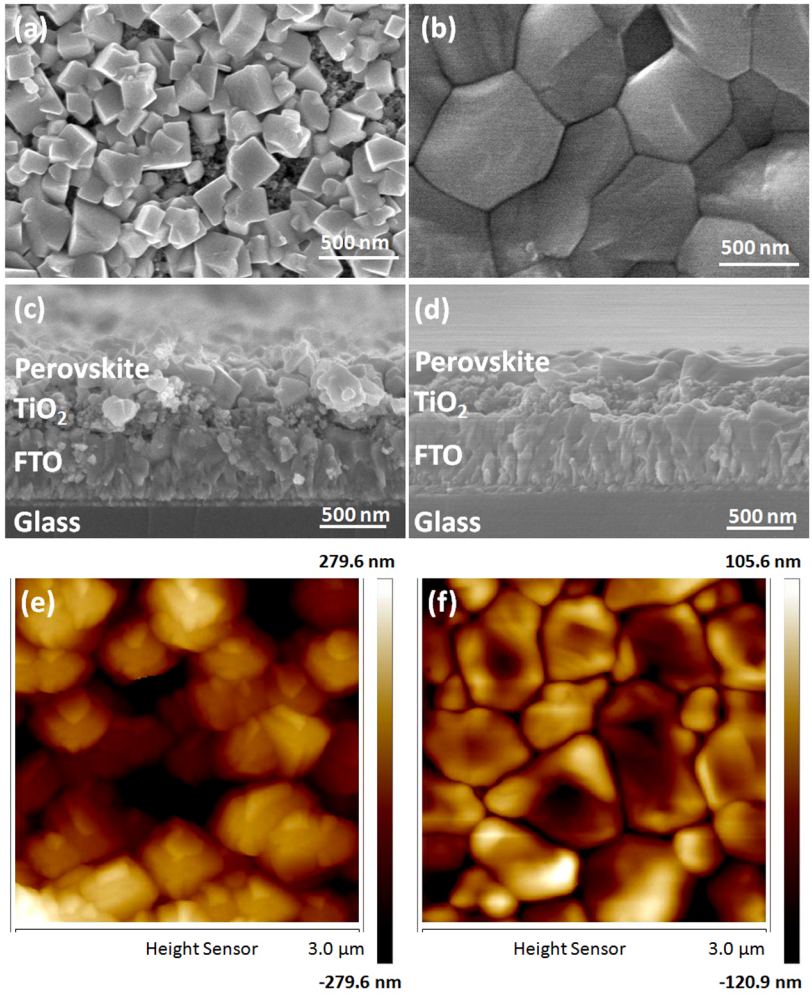

Figure 2. (a) Scanning electron microscope (SEM) topography, (c) cross-sectional SEM morphology, (e) atomic force microscopy (AFM) topography of the surface of sequential solution deposited perovskite film. (b) SEM topography, (d) cross-sectional SEM, and (f) AFM morphology of a gas−solid generated pinhole-free perovskite film.

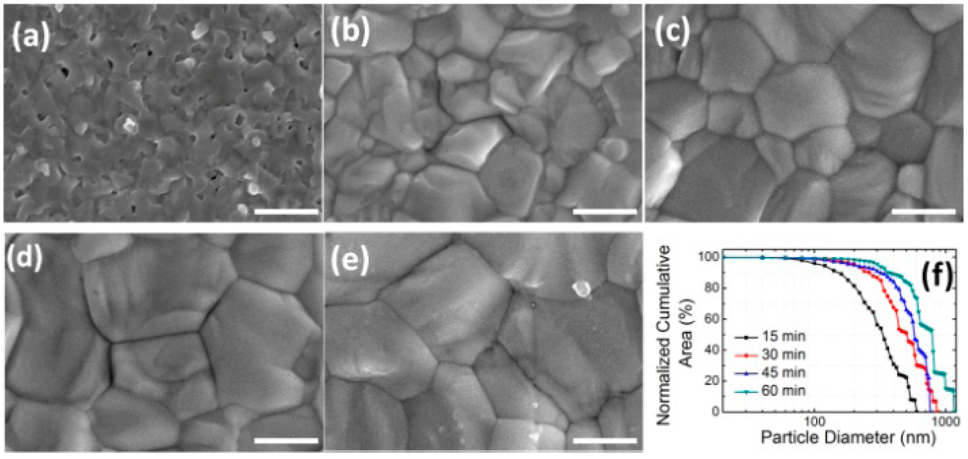

Figure 3. SEM topography of the perovskite films with a different reaction time of (a) 0 min, (b) 15 min, (c) 30 min, (d) 45 min, and (e) 60 min, and (f) the calculated particle size distributions. All scale bars represent 500 nm.

field generated in the ferroelectric perovskite layer has highlighted the importance of ferroelectric domains acting as "highways" for the transport of charge carriers.[43] Understandably, controlling the perovskite crystal growth will have a huge impact on controlling the interfaces between the subsequently deposited perovskite layers, in that the roughness of the hole conductor layer will depend on that of the perovskite layer. This is particularly true for planar heterojunction devices with no hole conductor layer, where a nonuniform perovskite layer would dramatically increase the

dx.doi.org/10.1021/ja509245x | J. Am. Chem. Soc. 2014, 136, 16411−16419

chance of charge carrier recombination. In our gas−solid crystallization process, the as-formed $CH_3NH_3PbI_3$ film exhibits full surface coverage and is composed of micrometer-sized grains as shown in Figure 2b. For comparison, a sequentially deposited $CH_3NH_3PbI_3$ film was also fabricated following the reported procedure.[4] Obviously, the crystal size of the sequential deposited $CH_3NH_3PbI_3$ is roughly estimated to be 200 ± 50 nm, which is much smaller as compared to that derived from gas−solid crystallization process. Meanwhile, bare TiO_2 surfaces can be observed in the sequential deposited perovskite films (Figure 2a), manifesting the film coverage is not complete.

The surface roughness of the film was further monitored by high-resolution atomic force microscopy (AFM) (Figure 2e and f). The size of the AFM images is 3 × 3 μm^2. The measured average roughness (R_a) and root-mean-square roughness (R_q) are 75.1 and 91.7 nm for the sequential deposited $CH_3NH_3PbI_3$ film and 26.3 and 32.8 nm for the gas−solid crystallized film regardless of its microscale grain size. Cross-sectional SEM images (Figure 2c and d) indicate both of the two resulting films have a comparable thickness of around 250 nm, with well-defined grains across the film thickness. Therefore, the full surface coverage, microscale grain size, and uniform grain structure of the as-formed perovskite film are highly suitable for planar heterojunction photovoltaic devices. These attractive characteristics arise from the combination of the relative smoothness of the preformed PbI_2 film, and the effective intercalation of CH_3NH_3I (or CH_3NH_2 + HI) vapor in it.

The crystal growth of the perovskite film is of major importance to fabricate efficient planar heterojunction devices, especially in the absence of the hole conductor layer. It is thus necessary to monitor the underlying thermodynamic mechanism of the crystal growth in perovskite thin-film though this gas−solid crystallization process. The perovskite film morphology evolution was investigated with an interval crystallization time of 15 min at a temperature of 150 °C in the nitrogen glovebox. As depicted in Figure 3a, the initial PbI_2/DMF intermediate film exhibits uniform polygon-shaped grains of a few hundred nanometers, as well as scattered voids among adjacent grains. The thickness of the initial film is around 200 nm. The particle size distributions (PSD) of the as-obtained perovskite films were further analyzed on the basis of the method introduced by Holzer et al.[44] More details can be found in the Supporting Information. After exposure to the CH_3NH_3I gas for 15 min, it converts to $CH_3NH_3PbI_3$ perovskite (without any PbI_2) from the evidence of XRD data. This indicates the formation of $CH_3NH_3PbI_3$ perovskite is greatly accelerated in the gas−solid interface as compared to the sequential solution deposition process, in which the unreacted PbI_2 peaks can still be seen for 1 h of reaction in isopropanol solution.[4] The accelerated crystal formation and growth rate may originate from the minimization of the diffusion limitation of the methylammonium iodide into the mesoporous TiO_2 pores at a gas−solid interface.

Notably, the $CH_3NH_3PbI_3$ films exhibit a full coverage on the mesoporous TiO_2 layer with a median grain size of 330 nm based on PSD analysis. The significantly enhanced grain size with respect to the PbI_2 precursor could be ascribed to volume expansion during the crystal growth from PbI_2 to perovskite by the intercalation of CH_3NH_3I, as well as rearrangement of the aggregated structure of PbI_2 driven by minimizing the grain boundary energy.[31] The absence of voids in the perovskite film is striking and suggests that the gas−solid crystallization promotes a facile rearrangement of PbI_2 and/or reorganization of PbI_2 framework via enhanced diffusion during film growth.[26,45] We observed that as the reaction time increases to 30, 45, and 60 min, micrometer-scale grains are observed in the perovskite films. In comparison to the original PbI_2 intermediate phase, the perovskite film differs in both morphology and size. The in-plane grain size of perovskite crystals is 3−4 times the film thickness, indicating that the growth of perovskite polycrystalline films mainly follows normal grain growth mode.[46] More interestingly, during crystallization of the perovskite film, a grain coarsening process is observed through motion of grain boundaries resulting in the shrinkage and elimination of small grains, which, in turn, results in an increase in the average size of the remaining grains (Figure 3f). Such grain coarsening is mainly driven by the reduction in the total grain boundary area and in the corresponding reduction in the total grain boundary energy that accompanies the area decrease.[46] It should pointed out that the calculated grain sizes are in fair agreement with those obtained from the XRD data using the peak width analysis. This analysis was carried out for the (022) reflection at 24.54°, which together with the (121) reflection are the only ones that are not split in the *I*4*cm* symmetry setting. Detailed analysis and tabulated data are provided in Supporting Information Figure S2 and Table S1, respectively.

Crystal Structures of the Intermediate Phases. To gain further insight into the perovskite film quality, we discuss the crystallite formation process with respect to different fabrication techniques. In the commonly applied one-step solution approach, despite the fact that several solvents have been employed for the dissolution of the $CH_3NH_3PbI_3$ perovskite such as dimethylformamide (DMF),[3] γ-butyrolactone (GBL),[13] and dimethyl sulfoxide (DMSO),[32] a common feature is always present: a needle-shaped morphology (Figure 4a) of the crystallites is preceded by the formation of an intermediate yellow phase with needle-shaped morphology. This phase is distinctively characterized by low angle X-ray diffraction reflections (typically $2\theta < 10°$), but the crystal structure has not been elucidated. In an attempt to contribute to the better understanding of these intermediates, we present the crystal structures of two such compounds in the context of this work. The first one, $CH_3NH_3PbI_3{\cdot}H_2O$, was obtained as thin, elongated, pale yellow needles from saturated $CH_3NH_3PbI_3$ solutions in concentrated hydriodic acid (HI, 57%) at ambient conditions. Similarly, $CH_3NH_3PbI_3{\cdot}$DMF was obtained as thin, elongated, pale yellow needles from saturated solutions of $CH_3NH_3PbI_3$ in DMF, also at ambient conditions. The former compound, $CH_3NH_3PbI_3{\cdot}H_2O$, first mentioned by Weber,[47] is metastable and spontaneously loses its crystalline water molecule converting to black, polycrystalline $CH_3NH_3PbI_3$ upon removal of the crystals from the mother liquor. Because of this behavior, we determined the crystal structure of the compound at −153 °C to prevent this structural transformation. The latter compound, $CH_3NH_3PbI_3{\cdot}$DMF, is relatively stable in air and converts only very slowly to black $CH_3NH_3PbI_3$ upon removal of the crystals from the mother liquor. For comparison, the DMSO−solvate variant is a completely stable intermediate up to 100 °C.[41] To highlight the universality of the tendency of the $CH_3NH_3PbI_3$ perovskite to incorporate a neutral small molecule accompanied by a profound change in its crystal structure, we mention the "ammonia bleaching" process, where the black perovskite films

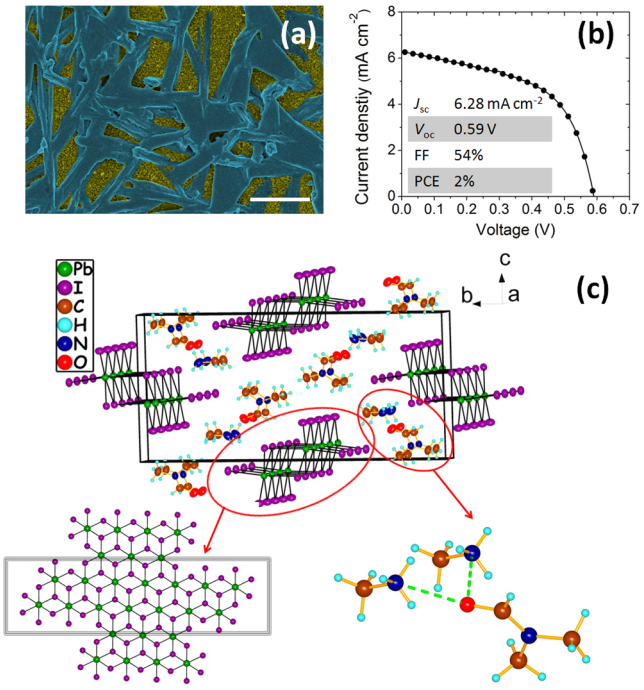

Figure 4. (a) SEM morphology of the perovskite film from one-step solution method. Scale bar represents 5 μm. (b) Corresponding current–voltage plots of the heterojunction devices in the absence of HTM. (c) The crystal structure of $CH_3NH_3PbI_3$·DMF highlighting the strong DMF–$CH_3NH_3^+$ interaction and the NH_4CdCl_3-type slab of the PbI_3^- chains. The boxed fragment indicates the relationship between the 2D layers of neat PbI_2 and the 1D PbI_3^- fragments of $CH_3NH_3PbI_3$·DMF.

can be reversibly converted to yellow upon exposure in NH_3 vapors.[48]

The crystal structure of the H_2O solvate consists of one-dimensional (1D) $\{PbI_3\}^-$ inorganic chains isolated from one another by $CH_3NH_3^+$ cations and water molecules crystallizing in the monoclinic $P2_1/m$ space group. The $\{PbI_3\}^-$ fragments adopt the "double-chain" assembly, which is reminiscent of the NH_4CdCl_3 structure-type characterized by three fused $[PbI_6]^{4-}$ octahedra sharing a common corner. In essence, these fragments are ribbons sliced from the layered PbI_2 structure (CdI_2 structure-type). The inserted $CH_3NH_3^+$ cations stabilize the negatively charged $\{PbI_3\}^-$ chains through electrostatic interactions. The guest H_2O molecules provide extra stabilization to the crystal structure by means of a strong symmetrically bifurcated H-bond ($d_{(N-O)}$ = 2.829 Å). In the case of $CH_3NH_3PbI_3$·DMF, the double-chain motif still dominates the configuration of the inorganic $\{PbI_3\}^-$ chain, which is surrounded by the $CH_3NH_3^+$ cations. The $CH_3NH_3^+$ cations are strongly H-bonded to a crystalline DMF molecule forming asymmetric bifurcated bonds with amide oxygen atom $d_{(N-O)}$ = 2.775 Å, $d_{(N'-O)}$ = 2.926 Å. The difference in the relative strength of the H-bonds in $CH_3NH_3PbI_3$·H_2O and $CH_3NH_3PbI_3$·DMF appears as a sensible explanation for the relative stability of the compounds at ambient conditions. Another difference between the H_2O and the DMF solvate is the doubling of the unit cell in the case of the bulkier, less symmetric DMF molecule, which possibly causes the lengthening of the unit cell along the crystallographic *c*-axis.

The structural motif adopted by the $\{PbI_3\}^-$ chains is very common in iodoplumbate chemistry, and it is observed in many $APbI_3$ compounds (A = NH_4, or an alkali metal). For example, this is the stable configuration of unsolvated $CsPbI_3$ and $RbPbI_3$[49] and the solvated forms of $KPbI_3$·$2H_2O$ and NH_4PbI_3·$2H_2O$ at ambient conditions.[50] Interestingly, the latter, unlike the $CH_3NH_3PbI_3$ solvates described above, adopt the dihydrate form rather than the monohydrate one. From the above crystal structures, a clear cation size effect is apparent with the largest cations stabilizing an anhydrous structure and the smallest ones a hydrated one. The size effect is also detrimental with respect to the formation of the NH_4CdCl_3-type or perovskites crystal structure. The borderline for the two structures lies between Rb and Cs because $CsPbI_3$ is able to adopt the perovskite at high temperature (~300 °C), whereas $RbPbI_3$ does not convert to a perovskite throughout the temperature range, below its melting point.[49] The above discussion on the structural correlations in $APbI_3$ highlights why the gas–solid crystallization method is very appealing and provides a consistent approach for the fabrication of robust perovskite layers in solid-state solar cells as we will show below. It avoids the complications associated with solvation and hydration processing and undesirable structural transitions.

Device Fabrication and Photovoltaic Performance. For the device preparation, a 30 nm-thick TiO_2 blocking layer was first deposited on the prepatterned FTO substrates by atomic layer deposition system. The mesoporous TiO_2 layer with a thickness of 250 nm was then deposited using a diluted TiO_2 paste in ethanol. Deposition of the $CH_3NH_3PbI_3$ perovskite layer was performed in two steps under nitrogen atmosphere. PbI_2 was first spin coated on the mesoporous TiO_2 layer from a 1 M DMF solution. The gas–solid crystallization process was carried at a temperature of 150 °C in a closed container with different reaction time to compare the grain size effect on the final device photovoltaic performance. Finally, the devices were completed by evaporating a thin gold layer (80 nm) on them as the back contact. For comparison, devices were also fabricated following the reported sequential deposition method with a reaction time of 5 min,[4] as well as the one-step deposition method from a mixed DMF solution of PbI_2 and CH_3NH_3I at a molar ratio of 1:1.[3]

Figure 5a shows the schematic image of the planar device structure (FTO glass/blocking TiO_2 layer/mesoporous TiO_2 layer/perovskite/Au) without the hole conductor layer. The light absorbance of these perovskite films was first probed by optical diffuse-reflectance measurements prior to the photovoltaic characterization as shown in Figure 5b. Impressively, the gas–solid crystallized film shows remarkably enhanced light harvesting in the long wavelength regime (650–800 nm), as evidenced by a much steeper absorption edge. Such an enhancement is attributed to the combined effect of high crystalline quality, well-defined crystal morphology, and excellent film coverage in the gas–solid interface crystallization process.

Figure 5c shows the current–voltage (J–V) characteristics of heterojunction perovskite solar cells based on the simple structure FTO/blocking TiO_2 layer/mesoporous TiO_2 layer/perovskite/Au with different grain size from the gas–solid crystallization. A reference cell fabricated with the one-step solution method was prepared for comparison, which displayed a short-circuit current density (J_{sc}) of 6.28 mA/cm^2, a V_{oc} of 0.59 V, and fill factor (FF) of 54%, resulting in a poor power conversion efficiency (PCE) of 2%, as shown in Figure 4b. As compared to the efficient perovskite solar cells, the significant drop in these parameters may be a result of poor coverage of

dx.doi.org/10.1021/ja509245x | J. Am. Chem. Soc. 2014, 136, 16411–16419

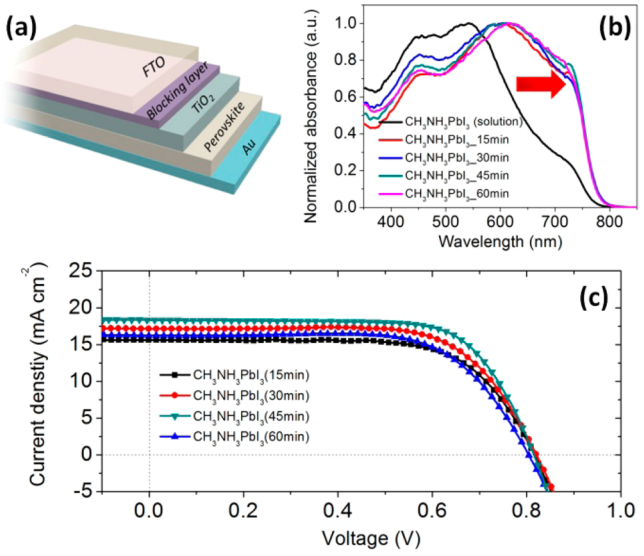

Figure 5. (a) Device architecture of the depleted heterojunction perovskite solar cell (FTO glass/blocking TiO_2 layer/mesoporous TiO_2 layer/perovskite/Au). (b) Normalized absorbance spectra of the perovskite films with different grain size. Absorbance spectrum of the sequential solution processed perovskite film is also presented for comparison. (c) Characteristic current–voltage plots of the heterojunction devices with different grain sized perovskite layers.

perovskite films. The effects of poor coverage are 2-fold: first, if there are regions with no perovskite coverage, light will pass through without absorption, decreasing the available photocurrent; second, any insufficient coverage results in a high frequency of "shunt paths" allowing contact between back electrode and the TiO_2 layer. Any such contact will act as a parallel diode in the solar cell equivalent circuit, causing a drop in V_{oc} and FF, and accordingly power conversion efficiency.[51,52]

With the superior perovskite film coverage of our process, all of the devices with gas–solid crystallized films show significant enhancement in the photovoltaic parameters. For instance, with an average gain size of 300 nm, device A delivers a J_{sc} of 15.75 mA/cm^2, a V_{oc} of 0.758 V, a FF of 68%, and a total PCE of 8.7%. We also notice a dependence of the perovskite grain size on the final photovoltaic performance. Both the J_{sc} and the FF slightly increased with the grain size growing from 300 to 600 nm, whereas the V_{oc} only marginally differed. Further increase of the grain size to approximately 600 nm increased the performance with a PCE of 10.6% under standard global AM 1.5 illumination. This enhancement originates from the enhanced crystalline orientation accompanying our crystal growth process. We also noticed that a further grain size increase to approximately 800 nm induced a slightly declined J_{sc} and V_{oc}. As recent studies have revealed the electron–hole diffusion length for $CH_3NH_3PbI_3$ perovskite is less than 1 μm,[14,15] a possible explanation for this decrease might be the limited charge collection efficiency in the cross-film direction of the perovskite particles.

Figure 6 shows the photovoltaic performance of the best-performing devices with these films. Devices with the gas–solid crystallized $CH_3NH_3PbI_3$ perovskite layer with a grain size of 550 nm deliver a J_{sc} of 18.33 mA/cm^2, a V_{oc} of 0.818 V, a FF of 71%, corresponding to an overall PCE of 10.6% under standard global AM 1.5 illumination, which is significantly higher than that from a sequential solution deposited perovskite film, with a J_{sc} of 15.48 mA/cm^2, a V_{oc} of 0.684 V, a FF of 60%, and a PCE of 6.4%. Notably, improvements are due to increased J_{sc}, V_{oc}, and FF, and are likely to stem from two effects resulting from improved perovskite film quality. First is the higher collection capability of a higher fraction of incident photons with higher surface coverage, increasing the current generated. Second, the increased coverage has reduced the contact area between the back electrode and the n-type TiO_2 layer, which removes a

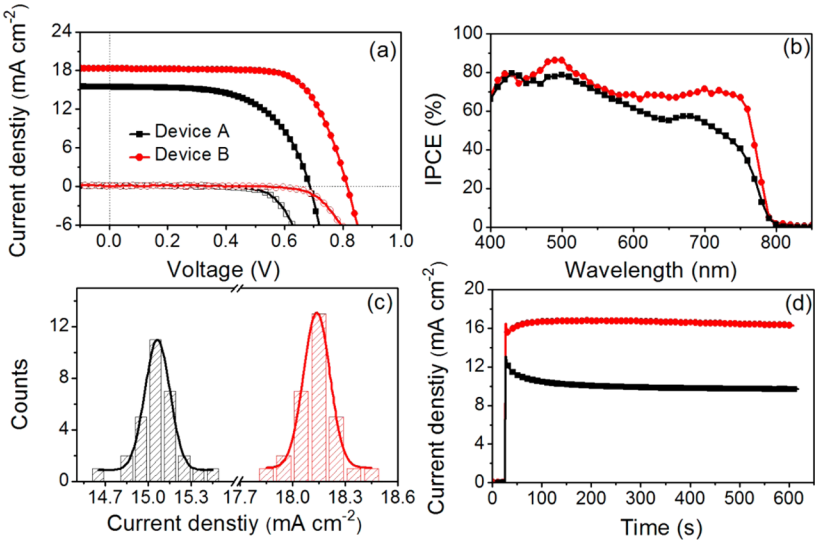

Figure 6. Comparison of the photovoltaic performance of the devices with the gas–solid generated and sequential solution deposited perovskite films. (a) Characteristic photocurrent–voltage and dark current–voltage plots. (b) The incident photon-to-current efficiency (IPCE) spectra for the best performing devices with the gas–solid crystallized and sequential solution deposited perovskite films. (c) Histogram of the short-circuit photocurrent density for a bath of 30 devices with the pinhole-free perovskite films (red) and the conventional sequential deposited films (black). (d) Comparison of the photocurrent density as a function of time for the cells held at a forward bias of maximum output power point (0.50 V for the device with a solution processed perovskite film and 0.62 V for that with a gas–solid crystallized perovskite film). The cell was placed in the dark prior to the start of the measurement.

dx.doi.org/10.1021/ja509245x | J. Am. Chem. Soc. 2014, 136, 16411–16419

shunt path previously leading to leakage currents.[51,52] Reduction of these shunt paths would therefore be expected to enhance the fill factor and V_{oc}. As evidently demonstrated by the dark current−voltage curves in Figure 6a, devices with perovskite films from our gas−solid crystallization process showed much higher dark current onset as compared to devices fabricated with the solution processed perovskite films. This is indicative of an effectively inhibited charge recombination in the former case.

Figure 6b shows the incident-photon-to-current conversion efficiency (IPCE) spectra for the perovskite cells from the gas−solid crystallization and the sequential deposition. The photocurrent generation starts at around 800 nm, in agreement with the observed band gap (E_g = 1.55 eV) of $CH_3NH_3PbI_3$,[53] and reaches a peak IPCE value of around 80% at 502 nm for the device with a sequential deposited film. The use of gas−solid crystallized perovskite film gave a noticeable improvement of the photocurrent over the whole region, especially in the long wavelength region between 600 and 800 nm due to more effective charge extraction and/or light harvesting. This IPCE enhancement correlates well with the higher light absorption in our thin films (Figure 5b). Integrating the overlap of the IPCE spectrum with the AM 1.5G solar photon flux yielded a photocurrent density of 17.98 and 15.17 mA/cm^2 for the gas−solid crystallization and sequential deposited perovskite film, which are in excellent agreement with the measured photocurrent density. This confirms that any mismatch between the simulated sunlight and the AM1.5G standard is negligibly small. To further check the reproducibility of the high efficient perovskite device without hole conductor layer, Figure 6c shows the histogram of the J_{sc} for a batch of 30 devices with the pinhole-free gas−solid crystallized perovskite films and the sequential deposited films. Obviously, the average J_{sc} value for the devices with gas−solid crystallized perovskite film is 18.14 ± 0.12 mA/cm^2, which is much higher than that of the sequential solution-deposited one at 15.07 ± 0.15 mA/cm^2. The small standard deviation indicates the good device reproducibility.

Recently, an anomalous hysteresis in the J−V curves of perovskite solar cells has been widely observed.[54−56] The hysteresis predominantly arises from the presence of the perovskite absorber in the solar cell, which is also dependent on the contact material, including p- and n-type contacts, and device architecture.[56] Monitoring the stabilized current density at the maximum output power point was widely recommended to provide more reliable photovoltaic performance alongside the current−voltage scan derived power conversion efficiency. We recorded the photocurrent density of two representative cells held at a forward bias near their maximum output power point as a function of time to monitor the stabilized power output under working conditions (Figure 6d). For the device with high-quality gas−solid crystallized perovskite film, the photocurrent density stabilizes within seconds to approximately 16.8 mA cm^{-2}, yielding a stabilized power conversion efficiency around 10.5%, measured after 600 s. This indicates that out test condition (from forward bias to short circuit scans with a scanning rate of 0.15 V s^{-1}) provides an accurate representation of the cells photovoltaic performance. However, a significant decay of the photocurrent from approximately 12.8 to 10.3 mA cm^{-2} was observed with the first hundred seconds under illumination, which then stabilized for the entire testing period. Such a photocurrent density decay could originate from the defects near the surface of perovskite or specifically generated interface states associated with solution process.[57] Therefore, we believe that the pinhole-free perovskite films from the gas−solid crystallization process provide a more stable stage for further efficiency improvement.

■ CONCLUSION

A fast, low temperature, gas−solid crystallization method has been described that enables the reproducible fabrication of high-quality perovskite films without pinholes. This allows better control over the dynamics of nucleation and crystal grain growth of $CH_3NH_3PbI_3$. Surface morphological analysis indicated that the perovskite films undergo a grain coarsening process, which is mainly driven by the reduction in the total grain boundary energy. This grain coarsening leads to a controllable grain size with full surface coverage of the resulting perovskite film. With respect to the conventional solution process, our gas−solid crystallization process effectively avoids the solvation and hydration processing or undesirable structural transitions. Taking advantage of these high-quality pinhole-free perovskite thin films, efficient planar heterojunction perovskite solar cells with no hole conductor materials can be fabricated. These films exhibit significant light harvesting enhancement in the long wavelength region and a considerably improved photocurrent density, as compared to conventional solution deposited films. Improvements in terms of open-circuit voltage and fill factor have also been achieved using these high-quality perovskite films, primarily due to the reduction of interfacial charge recombination with a fully covered perovskite film. A power conversion efficiency of over 10.6% has been realized with a negligible standard deviation. The present findings demonstrate that this gas−solid crystallization process is suitable for planar heterojunction perovskite solar cells, not only for the hole conductor free devices demonstrated in the present work, but also for other device architectures. It is anticipated that with further interfacial engineering, such as further facilitating the electron transport in TiO_2 media and hole extraction in perovskite solar cells, additional improvements in solar cell performance up to 20% are possible in HTM-free cells in the near future.

■ ASSOCIATED CONTENT

Supporting Information

Detailed experimental procedures and crystalline structure information on the salvation intermediates ($CH_3NH_3PbI_3$·DMF and $CH_3NH_3PbI_3$·H_2O), Figures S1−S7, and Tables S1−S11. This material is available free of charge via the Internet at http://pubs.acs.org.

■ AUTHOR INFORMATION

Corresponding Author

m-kanatzidis@northwestern.edu

Notes

The authors declare no competing financial interest.

■ ACKNOWLEDGMENTS

Electron microscopy analyses were done at the Electron Probe Instrumentation Center (EPIC) at Northwestern University. This research was supported as part of the ANSER Center, an Energy Frontier Research Center funded by the U.S. Department of Energy, Office of Science, Office of Basic Energy Sciences, under award no. DE-SC0001059.

REFERENCES

(1) Kojima, A.; Teshima, K.; Shirai, Y.; Miyasaka, T. *J. Am. Chem. Soc.* **2009**, *131*, 6050.
(2) Kim, H. S.; Lee, C. R.; Im, J. H.; Lee, K. B.; Moehl, T.; Marchioro, A.; Moon, S. J.; Humphry-Baker, R.; Yum, J. H.; Moser, J. E.; Gratzel, M.; Park, N. G. *Sci. Rep.* **2012**, *2*, 591.
(3) Lee, M. M.; Teuscher, J.; Miyasaka, T.; Murakami, T. N.; Snaith, H. J. *Science* **2012**, *338*, 643.
(4) Burschka, J.; Pellet, N.; Moon, S. J.; Humphry-Baker, R.; Gao, P.; Nazeeruddin, M. K.; Gratzel, M. *Nature* **2013**, *499*, 316.
(5) Chung, I.; Lee, B.; He, J. Q.; Chang, R. P. H.; Kanatzidis, M. G. *Nature* **2012**, *485*, 486.
(6) Etgar, L.; Gao, P.; Xue, Z. S.; Peng, Q.; Chandiran, A. K.; Liu, B.; Nazeeruddin, M. K.; Gratzel, M. *J. Am. Chem. Soc.* **2012**, *134*, 17396.
(7) Abu Laban, W.; Etgar, L. *Energy Environ. Sci.* **2013**, *6*, 3249.
(8) Borriello, I.; Cantele, G.; Ninno, D. *Phys. Rev. B* **2008**, *77*, 235214.
(9) Mitzi, D. B. *Prog. Inorg. Chem.* **1999**, *48*, 1−121.
(10) Kagan, C. R.; Mitzi, D. B.; Dimitrakopoulos, C. D. *Science* **1999**, *286*, 945.
(11) Noh, J. H.; Im, S. H.; Heo, J. H.; Mandal, T. N.; Seok, S. I. *Nano Lett.* **2013**, *13*, 1764.
(12) (a) Hao, F.; Stoumpos, C. C.; Cao, D. H.; Chang, R. P. H.; Kanatzidis, M. G. *Nat. Photonics* **2014**, *8*, 489. (b) Lee, B. Y.; Stoumpos, C. C.; Zhou, N. J.; Hao, F.; Malliakas, C. M.; Yeh, C. Y.; Marks, T. J.; Kanatzidis, M. G.; Chang, R. P. H. *J. Am. Chem. Soc.* **2014**, *136*, 15379−15385.
(13) Heo, J. H.; Im, S. H.; Noh, J. H.; Mandal, T. N.; Lim, C. S.; Chang, J. A.; Lee, Y. H.; Kim, H. J.; Sarkar, A.; Nazeeruddin, M. K.; Gratzel, M.; Seok, S. I. *Nat. Photonics* **2013**, *7*, 487.
(14) Xing, G. C.; Mathews, N.; Sun, S. Y.; Lim, S. S.; Lam, Y. M.; Gratzel, M.; Mhaisalkar, S.; Sum, T. C. *Science* **2013**, *342*, 344.
(15) Stranks, S. D.; Eperon, G. E.; Grancini, G.; Menelaou, C.; Alcocer, M. J. P.; Leijtens, T.; Herz, L. M.; Petrozza, A.; Snaith, H. J. *Science* **2013**, *342*, 341.
(16) Zhou, H.; Chen, Q.; Li, G.; Luo, S.; Song, T.-b.; Duan, H.-S.; Hong, Z.; You, J.; Liu, Y.; Yang, Y. *Science* **2014**, *345*, 542.
(17) Green, M. A.; Emery, K.; Hishikawa, Y.; Warta, W.; Dunlop, E. D. *Prog. Photovoltaics* **2014**, *22*, 701.
(18) Kim, H. S.; Lee, J. W.; Yantara, N.; Boix, P. P.; Kulkarni, S. A.; Mhaisalkar, S.; Gratzel, M.; Park, N. G. *Nano Lett.* **2013**, *13*, 2412.
(19) Liu, D. Y.; Kelly, T. L. *Nat. Photonics* **2014**, *8*, 133.
(20) Ball, J. M.; Lee, M. M.; Hey, A.; Snaith, H. J. *Energy Environ. Sci.* **2013**, *6*, 1739.
(21) Liu, M. Z.; Johnston, M. B.; Snaith, H. J. *Nature* **2013**, *501*, 395.
(22) Eperon, G. E.; Stranks, S. D.; Menelaou, C.; Johnston, M. B.; Herz, L. M.; Snaith, H. J. *Energy Environ. Sci.* **2014**, *7*, 982.
(23) Nayak, P. K.; Cahen, D. *Adv. Mater.* **2014**, *26*, 1622.
(24) Schulz, P.; Edri, E.; Kirmayer, S.; Hodes, G.; Cahen, D.; Kahn, A. *Energy Environ. Sci.* **2014**, *7*, 1377.
(25) Ponseca, C. S.; Savenije, T. J.; Abdellah, M.; Zheng, K. B.; Yartsev, A.; Pascher, T.; Harlang, T.; Chabera, P.; Pullerits, T.; Stepanov, A.; Wolf, J. P.; Sundstrom, V. *J. Am. Chem. Soc.* **2014**, *136*, 5189.
(26) Mitzi, D. B. *Chem. Mater.* **2001**, *13*, 3283.
(27) Liang, K. N.; Mitzi, D. B.; Prikas, M. T. *Chem. Mater.* **1998**, *10*, 403.
(28) Shi, J. J.; Dong, J.; Lv, S. T.; Xu, Y. Z.; Zhu, L. F.; Xiao, J. Y.; Xu, X.; Wu, H. J.; Li, D. M.; Luo, Y. H.; Meng, Q. B. *Appl. Phys. Lett.* **2014**, *104*, 063901.
(29) Rong, Y. G.; Ku, Z. L.; Mei, A. Y.; Liu, T. F.; Xu, M.; Ko, S. G.; Li, X.; Han, H. W. *J. Phys. Chem. Lett.* **2014**, *5*, 2160.
(30) Aharon, S.; Gamliel, S.; El Cohen, B.; Etgar, L. *Phys. Chem. Chem. Phys.* **2014**, *16*, 10512.
(31) Chen, Q.; Zhou, H. P.; Hong, Z. R.; Luo, S.; Duan, H. S.; Wang, H. H.; Liu, Y. S.; Li, G.; Yang, Y. *J. Am. Chem. Soc.* **2014**, *136*, 622.
(32) Wu, Y.; Islam, A.; Yang, X.; Qin, C.; Liu, J.; Zhang, K.; Peng, W.; Han, L. *Energy Environ. Sci.* **2014**, *7*, 2934.
(33) Era, M.; Hattori, T.; Taira, T.; Tsutsui, T. *Chem. Mater.* **1997**, *9*, 8.
(34) Matsushima, T.; Fujita, K.; Tsutsui, T. *Jpn. J. Appl. Phys.* **2006**, *45*, 523.
(35) Graetzel, M.; Janssen, R. A. J.; Mitzi, D. B.; Sargent, E. H. *Nature* **2012**, *488*, 304.
(36) Chen, Q.; Zhou, H.; Song, T.-B.; Luo, S.; Hong, Z.; Duan, H.-S.; Dou, L.; Liu, Y.; Yang, Y. *Nano Lett.* **2014**, *14*, 4158.
(37) Stoumpos, C. C.; Malliakas, C. D.; Kanatzidis, M. G. *Inorg. Chem.* **2013**, *52*, 9019.
(38) Cao, D. H.; Stoumpos, C. C.; Malliakas, C. D.; Katz, M. J.; Farha, O. K.; Hupp, J. T.; Kanatzidis, M. G. *APL Mater.* **2014**, *2*, 091101.
(39) Wakamiya, A.; Endo, M.; Sasamori, T.; Tokitoh, N.; Ogomi, Y.; Hayase, S.; Murata, Y. *Chem. Lett.* **2014**, *43*, 711.
(40) Beckmann, P. A. *Cryst. Res. Technol.* **2010**, *45*, 455.
(41) Jeon, N. J.; Noh, J. H.; Kim, Y. C.; Yang, W. S.; Ryu, S.; Seok, S. I. *Nat. Mater.* **2014**, *13*, 897.
(42) Roiati, V.; Mosconi, E.; Listorti, A.; Colella, S.; Gigli, G.; De Angelis, F. *Nano Lett.* **2014**, *14*, 2168.
(43) Frost, J. M.; Butler, K. T.; Brivio, F.; Hendon, C. H.; van Schilfgaarde, M.; Walsh, A. *Nano Lett.* **2014**, *14*, 2584.
(44) Munch, B.; Holzer, L. *J. Am. Ceram. Soc.* **2008**, *91*, 4059.
(45) Mitzi, D. B.; Prikas, M. T.; Chondroudis, K. *Chem. Mater.* **1999**, *11*, 542.
(46) Thompson, C. V. *Annu. Rev. Mater. Sci.* **2000**, *30*, 159.
(47) Poglitsch, A.; Weber, D. *J. Chem. Phys.* **1987**, *87*, 6373.
(48) Zhao, Y. X.; Zhu, K. *Chem. Commun.* **2014**, *50*, 1605.
(49) Trots, D. M.; Myagkota, S. V. *J. Phys. Chem. Solids* **2008**, *69*, 2520.
(50) Bedlivy, D.; Mereiter, K. *Acta Crystallogr., Sect. B* **1980**, *36*, 782.
(51) Docampo, P.; Snaith, H. J. *Nanotechnology* **2011**, *22*, 225403.
(52) Han, L. Y.; Koide, N.; Chiba, Y.; Mitate, T. *Appl. Phys. Lett.* **2004**, *84*, 2433.
(53) Hao, F.; Stoumpos, C. C.; Chang, R. P. H.; Kanatzidis, M. G. *J. Am. Chem. Soc.* **2014**, *136*, 8094.
(54) Kim, H. S.; Park, N. G. *J. Phys. Chem. Lett.* **2014**, *5*, 2927.
(55) Sanchez, R. S.; Gonzalez-Pedro, V.; Lee, J. W.; Park, N. G.; Kang, Y. S.; Mora-Sero, I.; Bisquert, J. *J. Phys. Chem. Lett.* **2014**, *5*, 2357.
(56) Snaith, H. J.; Abate, A.; Ball, J. M.; Eperon, G. E.; Leijtens, T.; Noel, N. K.; Stranks, S. D.; Wang, J. T. W.; Wojciechowski, K.; Zhang, W. *J. Phys. Chem. Lett.* **2014**, *5*, 1511.
(57) Kim, H. S.; Mora-Sero, I.; Gonzalez-Pedro, V.; Fabregat-Santiago, F.; Juarez-Perez, E. J.; Park, N. G.; Bisquert, J. *Nat. Commun.* **2013**, *4*, 2242.